Waste-derived incense stick ash as a SCM: Linking multiscale gel-pore evolution, strength, and eco-efficiency via 1H LF-NMR and

Developments in the Built Environment 27 (2026) 100999

Contents lists available at ScienceDirect

Developments in the Built Environment

journal homepage: www.sciencedirect.com/journal/developments-in-the-built-environment

Waste-derived incense stick ash as a SCM: Linking multiscale gel-pore evolution, strength, and eco-efficiency via ^{1}H LF-NMR and nanoindentation

Zi-jun Li [a], Zhi-hai He [a,b,*], Fu-qiang He [c], Hanbing Zhao [d], Juan Wang [e,**], Arezou Babaahmadi [e]

[a] Zhejiang Key Laboratory of Rock Mechanics and Geohazards, School of Civil Engineering, Shaoxing University, Shaoxing, 312000, China
[b] State Key Laboratory of Intelligent Deep Metal Mining and Equipment, Shaoxing University, Shaoxing, 312000, China
[c] School of Civil Engineering and Architecture, Xiamen University of Technology, Xiamen, 361024, China
[d] Centre for Infrastructure Engineering and Safety, School of Civil and Environmental Engineering, The University of New South Wales, NSW, 2052, Australia
[e] Department of Architecture and Civil Engineering, Chalmers University of Technology, Gothenburg, 41296, Sweden

ARTICLE INFO

Keywords:
Incense stick ash
Low-field nuclear magnetic resonance
Nanoindentation
Gel pores
C-S-H evolution

ABSTRACT

Effective utilization of incense stick ash (ISA) as a supplementary cementitious material requires a mechanistic understanding of its effects on pore evolution and performance. This study evaluates multiscale pore characterization by ^{1}H low-field nuclear magnetic resonance (LF-NMR), mercury intrusion porosimetry, nitrogen adsorption, and backscattered electron imaging using ISA-blended cementitious materials as a case study. LF-NMR matched nitrogen adsorption for gel pores and MIP for capillary pores, while covering a wider pore-size range. Its intraglobular, small gel and large gel pores tracked C-S-H development and corresponded to nanoindentation-derived low-, high- and ultra-high-density C-S-H, establishing a pore-phase-mechanical bridge. A Bayesian-regularized backpropagation neural network using these parameters predicted performance with errors below 10.60%. Strength-normalized cost and carbon analyses identified 5% ISA as most eco-efficient. These results support ISA as a cleaner SCM and offer a cross-scale framework for data-driven design of waste-derived cementitious materials.

Abbreviations

BSE	Backscattered electron imaging	LGP	Large gel pores
C_{cost}	Absolute total cost	MIP	Mercury intrusion porosimetry
CI	Strength-normalized carbon footprint	NREC	Non-renewable energy consumption
CP	Coral powder	PC	Portland cement
C_p	Strength-normalized cost	SCMs	Supplementary cementitious materials
C-S-H	Calcium silicate hydrate	SEM	Scanning electron microscopy
C_{weight}	Total CO_2 emissions	SGP	Small gel pores
E_e	Strength-normalized embodied energy	SP	Polycarboxylate-based high-range water reducer
GGBS	Ground granulated blastfurnace slag	SSP	Steel slag powder
GRA	Grey relational analysis	T_2	Transverse relaxation time
HD	High density	$\overline{T_2}$	Weighted T_2 value
IGP	Intraglobular pores	UHD	Ultra-high density
ISA	Incense stick ash	UP	Unhydrated particles
LD	Low density	WDP	White dolomite powder
LF-NMR	Low-field nuclear magnetic resonance		

(*continued on next column*)

(*continued*)

1. Introduction

Concrete is produced on an unprecedented scale (Xiao et al., 2025; Marinković et al., 2021), and its associated cement consumption contributes substantially to global CO_2 emissions (Peng and Unluer, 2023). Partially replacing cement with supplementary cementitious materials (SCMs) is an essential strategy for reducing the environmental footprint of construction materials (Li et al., 2025). Incense stick ash (ISA) is an emerging SCM derived from the residues generated by burning incense sticks. Although produced in large quantities, it remains underutilized. Previous studies have shown that ISA can partially replace cement and measurably influence strength and hydration properties, consistent with its high SiO_2 and Al_2O_3 contents and potential pozzolanic reactivity (He et al., 2024). However, its effects on microstructural evolution,

* Corresponding author. Zhejiang Key Laboratory of Rock Mechanics and Geohazards, School of Civil Engineering, Shaoxing University, Shaoxing, 312000, China.
** Corresponding author.
E-mail addresses: zhihaihe1981@126.com (Z.-h. He), juanw@chalmers.se (J. Wang).

https://doi.org/10.1016/j.dibe.2026.100999
Received 6 June 2026; Received in revised form 26 July 2026; Accepted 27 July 2026
Available online 28 July 2026

performance development, and overall eco-efficiency remain insufficiently understood. Accordingly, ISA is adopted here as a representative waste-derived SCM to explore its multiscale structure–performance relationship and utilization potential.

For waste-derived SCMs such as ISA, the evolution of multiscale pore systems plays a decisive role in hydration kinetics, transport behavior, and macroscopic performance. Accurate characterization of pore structure evolution is essential not only for clarifying the action mechanism of ISA, but also for supporting performance-oriented and resource-efficient material design. Several high-precision methods have been employed to analyze pore features, including backscattered electron imaging (BSE) (Lyu et al., 2019), mercury intrusion porosimetry (MIP) (Chen et al., 2024; Lam et al., 2024), and nitrogen (N_2) adsorption (Chen and Ye, 2024; Patel et al., 2021). For instance, BSE allows a quantitative assessment of the pore morphology and distribution in cement pastes (Lyu et al., 2019), whereas MIP provides the volumetric distributions of different pore types (Chen et al., 2024; Lam et al., 2024). Chen and Ye (Chen and Ye, 2024) employed N_2 adsorption to analyze the porosity of 90-day pastes. However, these methods have inherent limitations. The BSE captures only local features and cannot provide a holistic analysis of pore distribution. N_2 adsorption exhibits limited resolution for gel pores in the 1.5–2 nm range. The “ink bottle effect” may cause bias in the measurement results (Jiang et al., 2023). Moreover, these methods typically require drying, heating, or high-pressure pretreatment, which are time-consuming and costly and may irreversibly alter the original pore structure, compromising measurement fidelity. In summary, traditional methods are generally constrained by limited measurement ranges, static results, and destructive sampling, making the dynamic, non-destructive, and multiscale monitoring of cementitious pore structures challenging to achieve. In contrast, low-field nuclear magnetic resonance (LF-NMR) has emerged as an advanced technique for non-destructive pore structure characterization owing to its efficiency, non-invasiveness, and capability for multiscale quantitative analysis (Jiang et al., 2023; Nestle et al., 2007).

LF-NMR exploits hydrogen nuclei as probes to accurately reflect the quantity and state of water molecules in cement-based materials (Cano-Barrita et al., 2009). By measuring the transverse relaxation time (T_2) of water in pores and correlating T_2 with pore size through theoretical or empirical relationships, LF-NMR enables a quantitative pore size distribution analysis (Liu et al., 2021; Ectors et al., 2016). LF-NMR has been applied in the field of cement-based materials to characterize pore structures (Zhang et al., 2023a), including the assessment of porosity, pore connectivity, and tortuosity in cement pastes (Liu et al., 2024). Ma et al. (2023) developed a correlation model between porosity and compressive strength based on LF-NMR, highlighting its potential for predicting mechanical performance. To enhance the measurement precision and interpretive power, LF-NMR is often combined with complementary experimental methods and theoretical models. For example, Xue et al. (2020) employed MIP and LF-NMR to investigate the restoration of thermally damaged cement mortar under water curing, demonstrating the higher sensitivity of LF-NMR for pores smaller than 0.02 μm in diameter. Yin et al. (2024) integrated LF-NMR with fractal dimension theory, quantitatively linking T_2 distributions to pore structure and accurately describing microstructural spatial distributions and evolution. However, the applicability of LF-NMR and other pore structure characterization techniques mentioned above for cement-based materials deserves an in-depth comparison. More importantly, a critical interpretive gap remains. While LF-NMR can effectively resolve pore signatures in cement pastes, the correspondence between relaxation-derived pore classes and the underlying calcium silicate hydrate (C-S-H) gel nanostructure has not yet been clearly established, particularly for C-S-H phases with different packing densities. Consequently, the correlations between LF-NMR gel-pore metrics and macroscopic mechanical performance are often empirical rather than mechanistically grounded. Nanoindentation provides a complementary nanomechanical phase method by quantitatively distinguishing different C-S-H gel phases in cement paste. Accordingly, integrating nanoindentation with LF-NMR may offer a feasible way to map gel-pore characteristics onto the evolution of C-S-H phases, thereby enabling an interpretable link between the pore structure, gel-phase development, and strength.

Accordingly, this study uses an ISA-blended cement paste as a representative waste-derived SCM system to develop a cross-scale pore-phase-strength assessment method. LF-NMR is compared with N_2 adsorption, MIP, and BSE to examine the consistency and complementarity of these techniques across different pore size ranges. Beyond establishing LF-NMR as an effective multiscale pore probe, this study further explores the correspondence between LF-NMR-resolved gel-pore characteristics and the C-S-H mechanical phases measured via nanoindentation, thereby linking ISA-induced pore refinement to nanomechanical phase evolution and strength development. Finally, the physically interpreted pore parameters are used for strength prediction and strength-normalized sustainability assessment. Therefore, the principal contribution of this study is the translation of LF-NMR-derived pore signals from empirical geometric indicators into mechanics-relevant descriptors, providing a potentially transferable method for evaluating the microstructural evolution and performance of waste-derived blended binders.

2. Raw materials and test program

2.1. Raw materials

P·I 52.5 Portland cement (PC) and incense stick ash (ISA) were used as binders, with deionized water used for paste preparation. The ISA was collected from incense stick combustion residues, ball-milled, and subsequently sieved through a 75 μm mesh. According to previous characterization, ISA is mainly composed of SiO_2 and Al_2O_3, indicating its potential pozzolanic reactivity (He et al., 2024). The median particle sizes of PC and ISA were 17 μm and 12 μm, respectively. Scanning electron microscopy (SEM) observations demonstrated that the ISA particles were irregular, with rough surfaces and pronounced porosity (Fig. 1). The superplasticizer used was a polycarboxylate-based high-range water reducer (SP) with a water-reducing efficiency of 25%.

2.2. Mix design

Cement pastes were prepared by partially replacing PC with ISA at mass replacement levels of 0%, 5%, 10%, 15%, and 20%. The water-to-binder ratio was maintained at 0.20, and the SP was incorporated at 1% of the binder mass to ensure the adequate workability of the mixture.

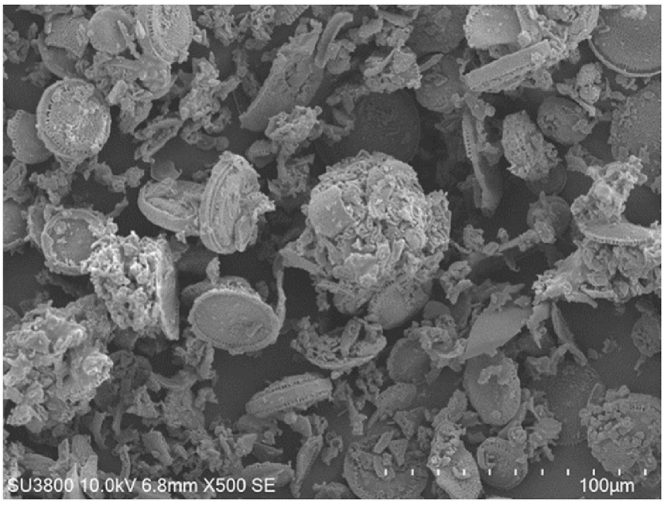

Fig. 1. SEM image of ISA.

The mixing proportions of the pastes are listed in Table 1. PC, ISA, and SP were initially dry-mixed for 1 min to achieve a uniform distribution. Water was then added gradually, while the mixture was stirred at a low speed for 120 s. After a 15 s pause, during which the material adhering to the mixer bowl and blade was scraped down, mixing was resumed at a high speed for another 120 s until a homogeneous paste was obtained. After mixing, the pastes were cast into 40 mm × 40 mm × 40 mm cubic molds, which were vibrated and leveled to ensure uniformity. The specimens were demolded after 24 h of curing at room temperature and subsequently cured in a standard curing chamber (20 ± 2 °C, 95% ± 3% RH) until the designated testing ages.

2.3. Methods

2.3.1. Compressive strength testing

The compressive strengths of the cubic specimens were determined according to the GB/T 17671 standard at curing ages of 1, 3, 7, 28, 60, and 90 days. A TENSON 600 kN servo-hydraulic testing machine was used with a loading rate of 2400 N/s. A minimum of six specimens per group was tested, and the average values were reported.

2.3.2. ^1H LF-NMR

^{1}H LF-NMR spectroscopy (NMRC12-010-T, Niumag Co., China) was used to monitor the state and relative content of water in the pastes at different curing ages. The instrument operated at a magnetic field strength of 0.28 T and a frequency of 11.9 MHz, using a 25 mm diameter coil. Freshly mixed pastes were cast into Φ5 mm × H20 mm cylindrical molds, sealed immediately to prevent water evaporation, and transferred to an NMR tube for measurement. The magnet bore temperature was maintained at 30 ± 0.01 °C. Tests were conducted on specimens cured under standard conditions at the corresponding ages, and the surface water signals were excluded from the analysis. The T_2 relaxation time ranges for different types of pore water are as follows: gel water (~0.01–1 ms), capillary water (~1–100 ms), and surface water (~100–10000 ms), with surface water including free water in fine pores and cracks (She and Yao, 2010). The relaxation spectra typically consisted of gel water, main water, and surface water peaks. Prior to the final setting, transitional peaks may appear between the main and surface water peaks (Ji et al., 2015). After setting, the gel and capillary water peaks merged into a single peak (Zeng et al., 2026).

2.3.3. BSE

BSE analysis was performed using an SU3800 SEM. The specimens were gold-coated before testing at an accelerating voltage of 15.0 kV and an image magnification of 500×. Three primary phases were identified in the raw images: unhydrated cement, hydration products, and pores, which exhibited sequential decreases in brightness. Image-Pro Plus 6.0 software was used to quantify the phase contents and determine the porosity and hydration degree of the samples. Twenty images per sample were analyzed and averaged to enhance the statistical reliability.

2.3.4. N_2 adsorption

The pore size distribution was measured using a Micromeritics-3020 porosimeter (USA). Samples were crushed into approximately 5 mm × 5 mm pieces, pretreated at 100 °C, and tested at 77 K using high-purity N_2 gas (>99.99%).

Table 1
Mix proportions of mixtures (g).

Group	PC	ISA	Water	SP
CP-ISA0	450.0	0.0	90.0	4.5
CP-ISA5	427.5	22.5	90.0	4.5
CP-ISA10	405.0	45.0	90.0	4.5
CP-ISA15	382.5	67.5	90.0	4.5
CP-ISA20	360.0	90.0	90.0	4.5

2.3.5. MIP

Specimens cured for 28 days were crushed into 3 mm–5 mm pieces, vacuum-dried, and tested using an Autopore IV 9500 instrument. The maximum applied pressure was 420 MPa, corresponding to a measurable pore size range of about 3 nm–400 μm.

2.3.6. Nanoindentation

Nanoindentation was performed using a Hysitron Ti-Premier nanoindenter to characterize the nanoscale mechanical properties of C-S-H gels and associated hydration phases (Hay et al., 2020; Sun et al., 2022; Sorelli et al., 2008). The central regions of the 28-day specimens were cut into 10 mm cubes and polished to a surface roughness of less than 100 nm. A 10 × 10 grid was used with a 10 μm spacing between the indents. The detailed testing procedures are provided in reference (He et al., 2024). The loading regime was configured as follows: 5 s of load application, followed by a 2 s holding period, and concluding with a 5 s unloading phase. The load was set at 2000 μN.

3. Results

3.1. Hydration evolution by LF-NMR

Liu et al. (2021) demonstrated that the weighted T_2 value ($\overline{T_2}$) can be used as an effective indicator of hydration progression, as defined in Eq. (1). In the present study, the temporal evolution of $\overline{T_2}$ was employed to monitor the hydration process of cement pastes. Fig. 2 presents the variation in $\overline{T_2}$ for samples at different curing ages. As hydration progressed, $\overline{T_2}$ gradually decreased, reflecting the continuous formation of hydration products that filled the pores and reduced the free water content. At 1 day, a pronounced decline in $\overline{T_2}$ indicated rapid refinement and filling of pore space during the early hydration stage. The different $\overline{T_2}$ curves observed among the mixtures containing ISA demonstrate that LF-NMR is sufficiently sensitive to capture variations in the early hydration behavior arising from changes in binder composition. The $\overline{T_2}$ values continued to decline for all samples at later ages. For instance, CP-ISA5 exhibited reductions of 4.11% and 43.93% compared to CP-ISA0 at 28 and 90 days, respectively. These differences illustrate that LF-NMR can effectively distinguish long-term hydration evolution in systems with ISA. By 90 days, the $\overline{T_2}$ value of CP-ISA20 approached that of the control paste (CP-ISA0), suggesting a convergence in hydration development at later stages.

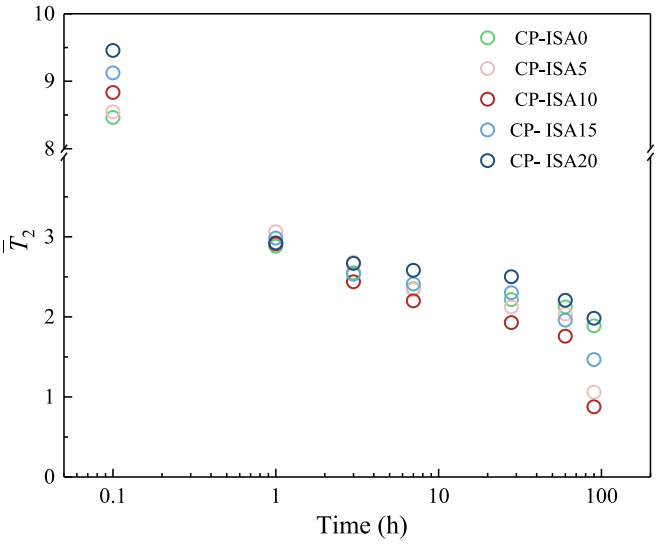

Fig. 2. $\overline{T_2}$ of cement paste at different curing ages estimated by LF-NMR.

$$\overline{T_2} = \frac{\int_0^{T_{MS}} T_2 I_{T_2} d\lg T_2}{\int_0^{T_{MS}} I_{T_2} d\lg T_2} \quad (1)$$

Where, T_{MS} denotes the minimum relative intensity of T_2 at the intersection between the surface water peak and other overlapping peaks (used to distinguish surface water from bulk T_2 peaks), and T_2 and I_{T2} represent the transverse relaxation time and its corresponding intensity, respectively.

3.2. Multi-technique pore structure characterization

3.2.1. BSE analysis

BSE images were segmented using grayscale thresholds determined by the overflow method to distinguish unhydrated cement particles, hydration products, and pores. Fig. 3(a) shows the 28-day porosity of the hardened pastes. The porosities of CP-ISA0, CP-ISA5, and CP-ISA20 were 11.24%, 8.43%, and 12.92%, respectively, indicating that ISA incorporation altered the pore features of the cement pastes. The corresponding hydration degrees, calculated using Eq. (2), were 77.36%, 80.92%, and 67.92%, respectively (Fig. 3(b)). The higher hydration degree and lower porosity of CP-ISA5 suggest that a low ISA replacement level promoted microstructural densification, whereas excessive ISA incorporation reduced the degree of hydration and increased porosity. Owing to its limited spatial resolution and two-dimensional imaging nature (Georget et al., 2024), BSE mainly provides trend-level microstructural evidence and was therefore used here as a complementary method for validating the pore-structure evolution identified by other techniques.

$$\alpha = (1 - A_{un}) \times 100\% \quad (2)$$

Where, α is the degree of hydration at 28 days and A_{un} denotes the area fraction of unhydrated cement particles within the analyzed region.

3.2.2. MIP

Cement paste pores are conventionally categorized as gel pores (<10 nm), capillary pores (10–1000 nm, subdivided into small capillaries: 10–100 nm and large capillaries: 100–1000 nm), and air voids (>1000 nm) (He et al., 2017). Gel pores are intrinsic components of the C-S-H nanostructure, arising from the irregular spacing generated during the stacking of C-S-H layers (Kunhi et al., 2020). In contrast, capillary pores are generally defined as the spaces left unfilled by hydration products after the initial mixing water and clinker particles dissolve. Therefore, they are classified as non-gel pores (Powers et al., 1959). The total pore volumes of CP-ISA0, CP-ISA5, and CP-ISA20 were 0.0178, 0.0163, and 0.0211 mL/g (Fig. 4), respectively. CP-ISA5 exhibited the lowest total pore volume, together with an increased gel-pore fraction and a reduced capillary-pore fraction, indicating that a low ISA replacement level refined the pore structure. In contrast, CP-ISA20 showed the highest total pore volume, suggesting that excessive ISA incorporation weakened pore refinement, probably because of the dilution effect (You et al., 2026). Although MIP effectively captured the relative refinement or coarsening of the capillary pore network, its interpretation of nanoscale gel pores is affected by the ink-bottle effect and high intrusion pressure (Georget et al., 2024). Therefore, the MIP results were mainly used to validate capillary-pore evolution and were further compared with N_2 adsorption and LF-NMR.

3.2.3. Nitrogen adsorption

N_2 adsorption was used to further characterize accessible nanoscale pores, particularly gel pores and fine capillary pores. As shown in Fig. 5, the total pore volumes of CP-ISA0, CP-ISA5, and CP-ISA20 were 0.02581, 0.02161, and 0.02994 cm^3/g, respectively. CP-ISA5 showed a lower total pore volume and reduced capillary-pore volume than CP-ISA0, indicating that a low ISA replacement level refined the nanoscale pore structure. In contrast, CP-ISA20 exhibited increased total and capillary-pore volumes, suggesting that excessive ISA incorporation increased capillary porosity. These trends were consistent with the MIP results, confirming that moderate ISA addition promoted pore refinement, whereas excessive replacement weakened the densification effect. Thus, N_2 adsorption provided nanoscale evidence for cross-validating the pore-structure evolution identified by MIP and LF-NMR.

3.2.4. LF-NMR

Using the Carr–Purcell–Meiboom–Gill (CPMG) sequence, the LF-NMR T_2 signals were transformed into pore structure parameters for quantitative analysis (Zhan et al., 2024; Zhou et al., 2017), as described by Eq. (3).

$$\frac{1}{T_2} \approx \frac{\delta}{T_{2S}} \cdot \frac{S_C}{v_w} = \frac{\delta}{T_{2S}} \cdot \frac{4}{D} = \gamma \cdot \frac{4}{D} \quad (3)$$

Where, δ is the solid surface area, T_{2s} is the transverse relaxation time of the surface water, υ_ω is the total pore water volume, γ is the relaxation constant (5.51 μm/s (Zhan et al., 2024)), and D is the pore diameter.

Fig. 6 presents the LF-NMR-derived pore size distributions at multiple curing ages, primarily identifying the gel and capillary pores. Across all mixtures, the pore network evolved substantially with the hydration time. At 28 days, CP-ISA5 exhibited a 13.64% reduction in total porosity and a 15.98% decrease in capillary pores compared with the control. At 90 days, the gel-pore fraction increased by 11.18%, whereas the total porosity and capillary pores decreased by 7.61% and 15.98%, respectively. These results illustrate that LF-NMR effectively captures the temporal evolution of the pore system and provides a coherent description of pore evolution that aligns with the trends observed in the MIP and N_2 adsorption results.

3.3. Nanoindentation

The type and content of hydration products profoundly influence the macroscopic and mechanical properties of cement pastes (He et al.,

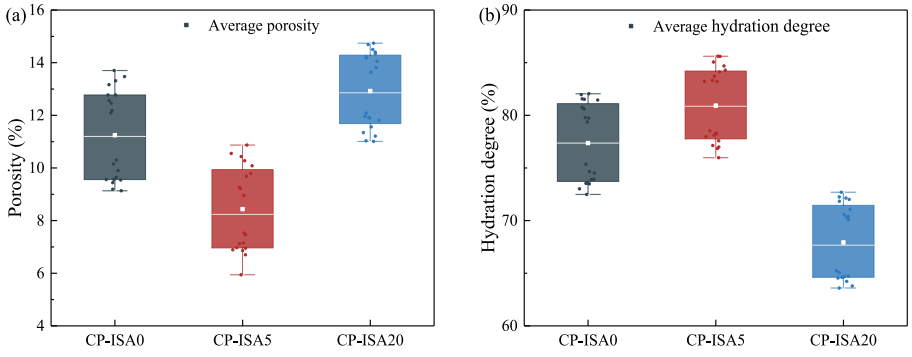

Fig. 3. Porosity (a) and hydration degree (b) of samples with varying ISA contents at 28 days.

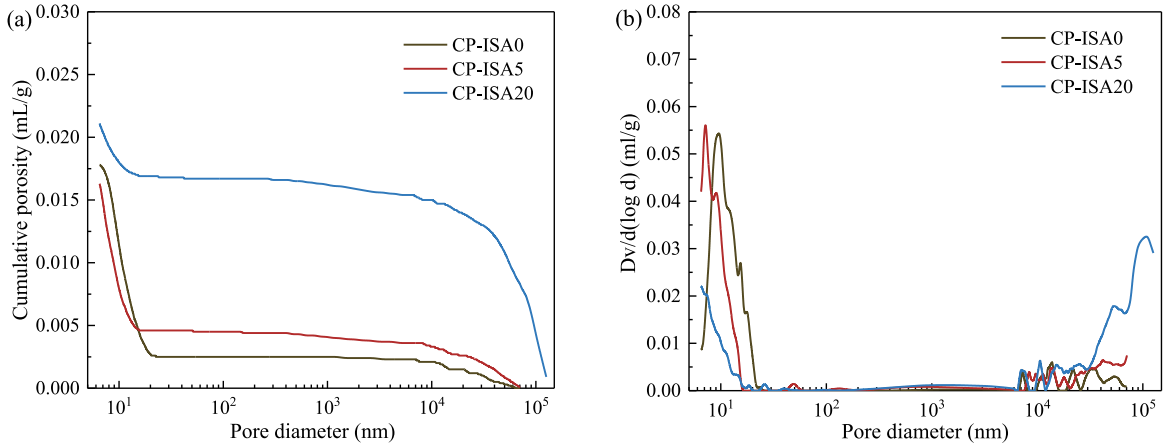

Fig. 4. Pore structure of samples at 28 days measured by MIP, cumulative porosity (a) and pore distribution (b).

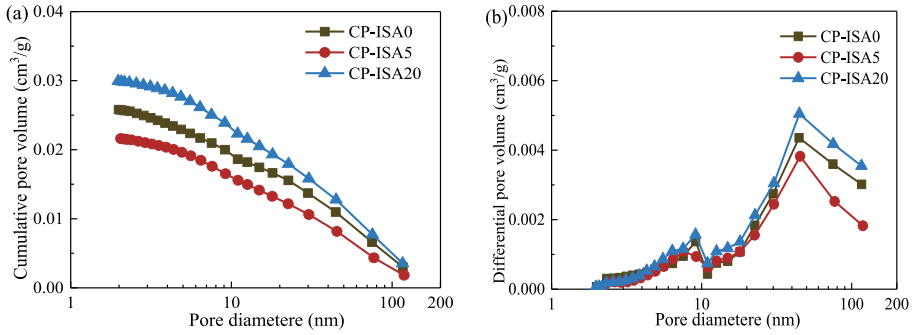

Fig. 5. Pore structure of samples at 28 days measured by N_2 adsorption, cumulative porosity (a) and pore distribution (b).

2022; Liu et al., 2026). The indentation modulus derived from the Oliver-Pharr analysis was converted to the elastic modulus (E) using Eq. (4) (Zhang et al., 2023b). Following previous studies (He et al., 2022), the elastic modulus can be used to distinguish between the different constituent phases of the paste. The different phases can be classified as pores (≤8 GPa), C-S-H gel (8–50 GPa), and unhydrated particles (UP, ≥50 GPa). The elastic moduli of low density (LD) C-S-H gel, high density (HD) C-S-H gel, and ultra-high density (UHD) C-S-H gel are considered to be in the ranges of 8–20 GPa, 20–34 GPa, and 34–50 GPa, respectively.

By statistically analyzing the frequency distribution of the nano-indentation measurements and fitting them with Gaussian components, the elastic modulus and volume fraction of each phase were determined (Fig. 7). The analysis assumes that the paste consists of N mechanically distinct phases and that the modulus values of each phase follow a Gaussian distribution, as expressed in Eq. (5) (Zhang et al., 2023b). Accordingly, the measured modulus distribution can be formulated as a superposition of the phase-level probability density functions, as shown in Eqs. (6) and (7) (Zhang et al., 2023b). Specifically, a frequency histogram of the elastic modulus E was constructed from the indentation dataset and decomposed in Origin using a multi-peak (N = 5) Gaussian fitting. The five components were assigned to the pores, LD C-S-H, HD C-S-H, UHD C-S-H, and UP phases.

$$\frac{1}{E_r}=\frac{1-\nu^2}{E}+\frac{1-\nu_0^2}{E_0} \tag{4}$$

Where, E and ν are the elastic modulus and Poisson's ratio of the tested material, E_0 and ν_0 are the elastic modulus and Poisson's ratio of the indenter, respectively, and E_r is the indentation modulus of the material.

$$p\left(E|\mu_j,\sigma_j\right)=\frac{1}{\sigma_j\sqrt{2\pi}}EXP\left(\frac{-\left(E-\mu_j\right)^2}{2{\sigma_j}^2}\right) \tag{5}$$

$$P(E)=\sum_{j=1}^{N}f_j \tag{6}$$

$$\sum_{j=1}^{N}f_j=1 \tag{7}$$

Where, μ_j and σ_j are the mean and standard deviation of the j phase, respectively, *and* f_j is the surface fraction occupied by the phase j on the indented surface.

Across all mixtures, UP exhibited the highest frequency, followed by C-S-H gel, which is consistent with the low water-to-binder ratio and substantial amount of residual anhydrous phases that are typically present in dense pastes. The incorporation of 5% ISA decreased the relative fractions of the pore phases and UP while increasing the fraction of C-S-H gel. Compared with the control, CP-ISA5 showed increases of 18.18% and 20.83% in the fractions of HD and UHD C-S-H, respectively. These C-S-H gels exhibit higher stiffness and lower deformability than LD C-S-H, thereby contributing more prominently to the load-bearing skeleton of the hardened matrix. At 20% ISA, the fractions of the pore phases and UP increased, whereas the proportion of C-S-H gel decreased significantly. Overall, nanoindentation effectively captured the nano-mechanical signatures associated with phase evolution and provided a complementary perspective to pore-structure characterization methods, enabling a consistent interpretation of microstructural evolution across scales and providing a basis for subsequently establishing the relationship between gel pores and strength.

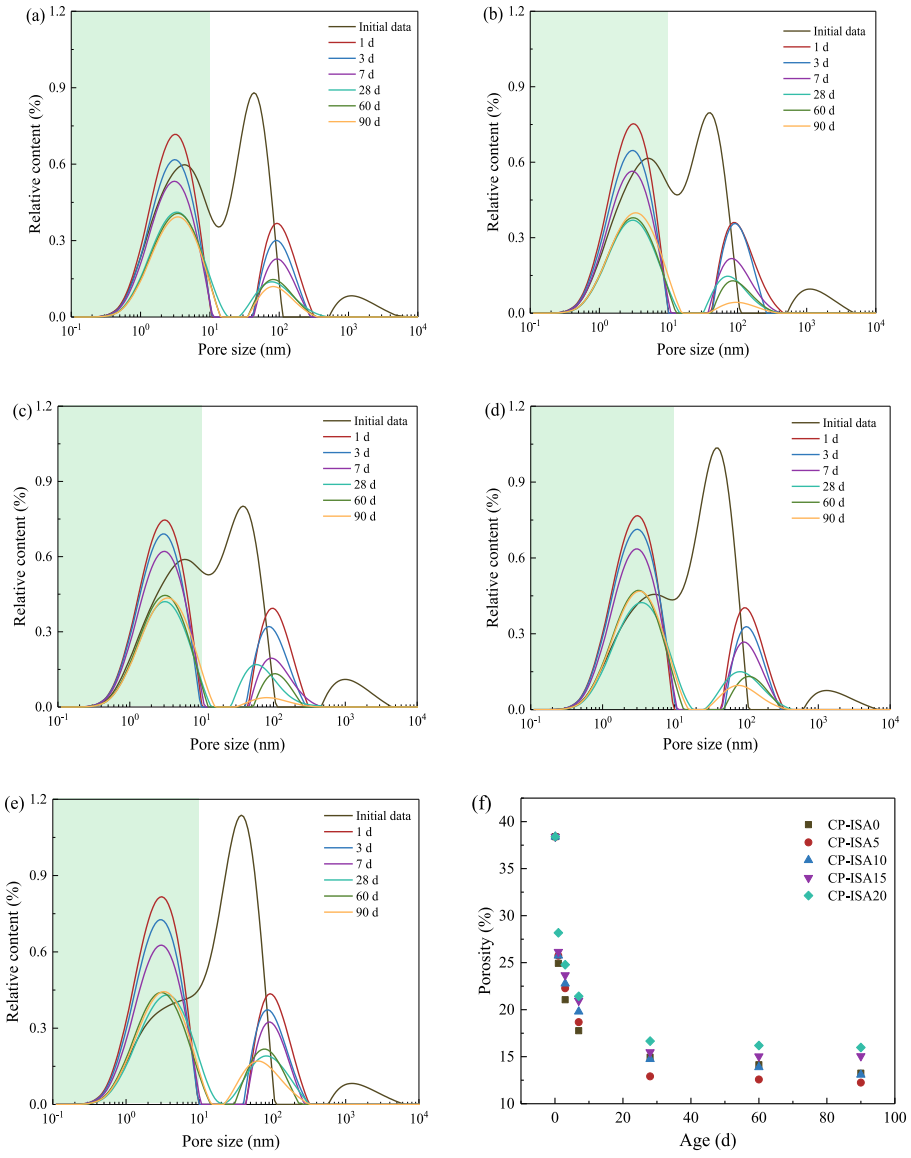

Fig. 6. Pore size distribution of samples measured by LF-NMR, CP-ISA0 (a), CP-ISA5 (b), CP-ISA10 (c), CP-ISA15 (d), CP-ISA20 (e), and total porosity (f).

3.4. Compressive strength

Fig. 8 illustrates the compressive strengths and corresponding growth rates of the pastes containing different ISA contents from 1 to 90 days. At 1 and 3 days, the CP-ISA5 mixture exhibited lower strength than the control (CP-ISA0), although the difference became negligible by 7 and 28 days. By 90 days, CP-ISA5 surpassed the control by 5.16%. In contrast, CP-ISA20 exhibited consistently lower strengths than the control across all curing ages, reaching 93.52% of the strength of CP-ISA0 at 90 days. Nevertheless, CP-ISA20 demonstrated a pronounced strength improvement of 115.63% between 1 and 90 days, indicating sustained hydration and progressive microstructure development.

The strength evolution can be attributed to the combined effects of clinker dilution, filler action, and pozzolanic reaction, as schematically illustrated in Fig. 9. At early ages, ISA mainly acts as a low-reactivity filler, and the reduced clinker content limits early hydration product formation, resulting in lower early strength. At later ages, the pozzolanic reaction of reactive SiO_2 and Al_2O_3 consumes $Ca(OH)_2$ and forms additional C-S-H, promoting matrix densification. Thus, a moderate ISA content increases the fractions of HD and UHD C-S-H and improves long-term strength. However, excessive ISA replacement reduces $Ca(OH)_2$ availability, restricts secondary hydrate formation, increases porosity, and consequently weakens mechanical performance.

4. Discussion

4.1. LF-NMR validation and C-S-H/gel pore evolution

N_2 adsorption mainly probes accessible nanoscale gel pores, while MIP reflects the entry diameters of mercury-accessible capillary pores. By detecting hydrogen-bearing pore water, LF-NMR covers a broader pore-size range. The 28-day pore size distributions showed excellent agreement between LF-NMR and N_2 adsorption in the gel-pore range and between LF-NMR and MIP in the capillary-pore range, both with ($R^2 = 0.99$) (Fig. 10). LF-NMR also detected interlayer water below approximately 2 nm, which is difficult to quantify by conventional methods and should not be strictly treated as porosity (Georget et al., 2024). These results validate LF-NMR as a reliable multiscale pore characterization tool for linking pore evolution with C-S-H structure and mechanical performance.

Gel-pore volume was used as an indirect indicator of C-S-H development because of its positive correlation with C-S-H gel content (Lu

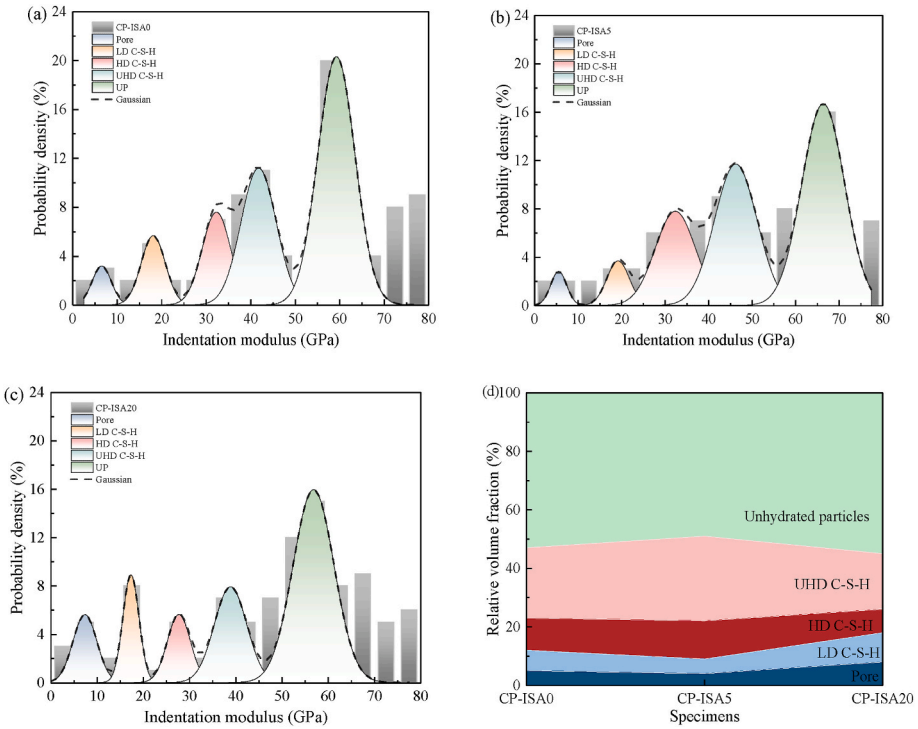

Fig. 7. Frequency distributions of the elastic modulus at 28 days for CP-ISA0 (a), CP-ISA5 (b), and CP-ISA20 (c), along with the volume fractions of the constituent phases (d).

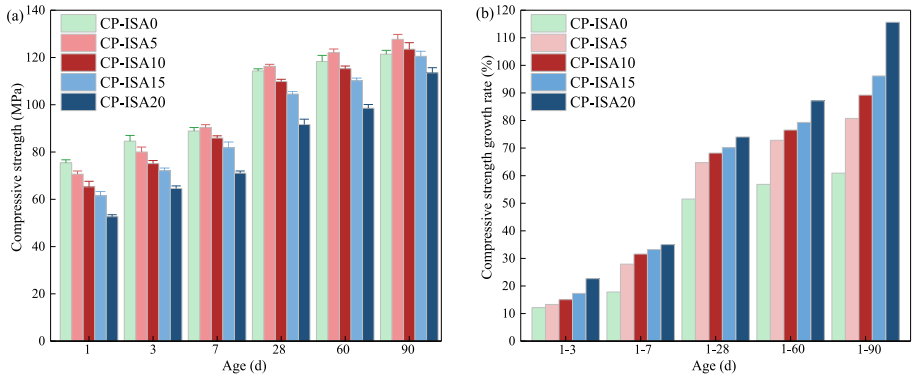

Fig. 8. Compressive strengths (a) and growth rates (b) of samples with different ISA contents.

et al., 2021). C-S-H gel pores are commonly classified as intraglobular pores (IGP, ≤1 nm), small gel pores (SGP, 1–3 nm), and large gel pores (LGP, 3–12 nm), reflecting the packing and refinement of the gel structure (Jennings, 2008). Compared with conventional techniques, which are limited by phase overlap and weak compositional contrast (Lothenbach et al., 2011), LF-NMR enables quantitative estimation of IGP, SGP, and LGP fractions, thereby supporting the analysis of C-S-H gel-pore evolution.

Fig. 11 shows the gel-pore distributions of the pastes from 1 to 90 days. CP-ISA0 maintained a relatively high LGP fraction, whereas ISA-containing pastes showed more evident redistribution from LGP toward finer gel pores. At early ages, ISA incorporation increased the IGP and SGP fractions while reducing the LGP fraction, indicating accelerated gel-pore refinement. At 28 days, CP-ISA5 and CP-ISA10 exhibited the most pronounced refinement, with higher IGP and SGP fractions than both the control and the high-ISA mixtures. In contrast, CP-ISA15 and CP-ISA20 retained higher LGP fractions, suggesting that excessive ISA delayed the densification of the C-S-H gel structure. At 90 days, all ISA-containing pastes still showed higher IGP fractions and lower LGP fractions than CP-ISA0, confirming sustained gel-pore refinement. Overall, LF-NMR quantitatively captured the progressive transformation from larger to finer gel pores, providing pore-scale evidence for linking C-S-H structural evolution with nanomechanical phase development.

4.2. *Linking pore structure to nanomechanical properties*

Based on the multiscale pore characterization in Section 4.1, grey relational analysis (GRA) was first used to identify the LF-NMR-derived pore parameters most closely related to compressive strength. Compressive strength was set as the reference sequence, while pore structure parameters at different ages were used as comparison sequences, with the resolution coefficient ρ set to 0.5. As shown in Table 2, total porosity, LGP, SGP, and IGP showed the highest grey relational degrees with compressive strength, followed by pores of 12–50 nm, 50–100 nm, and >100 nm. The weaker correlations of pores larger than 50 nm indicate that strength development is more closely associated with gel-pore refinement and overall pore densification than with coarse capillary pores. However, these statistical correlations alone do not

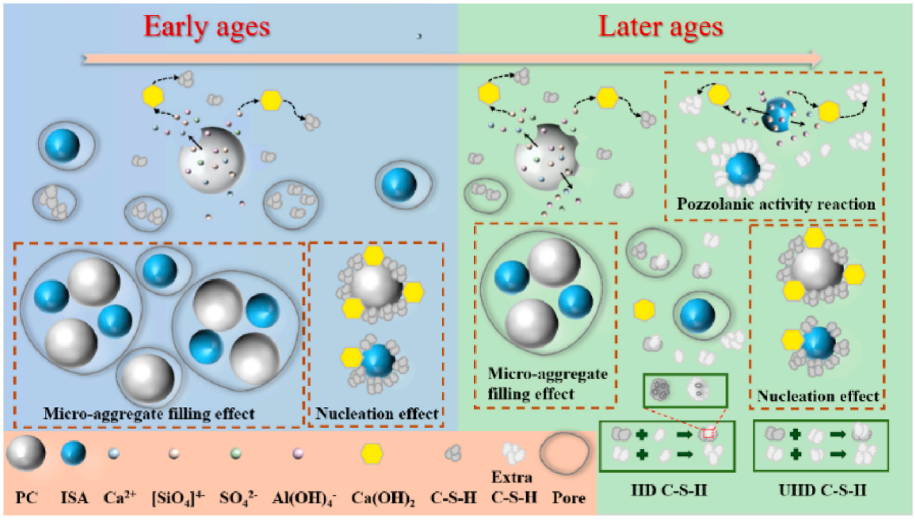

Fig. 9. Schematic illustration of the effects of ISA on the performance development of cement paste.

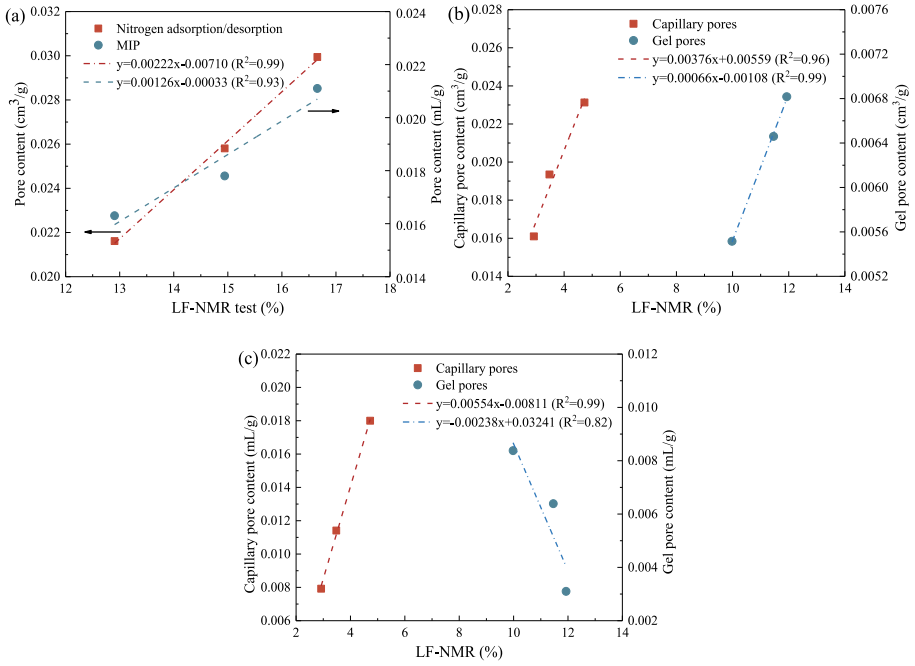

Fig. 10. Comparison of total (a), gel, and capillary porosities based on LF-NMR, N_2 adsorption (b), and MIP (c).

confirm whether the LF-NMR-derived gel-pore parameters have clear physical relevance to strength development.

$$\xi_i(k) = \frac{\min_i \min_k \Delta_i(k) + \rho \max_i \max_k \Delta_i(k)}{\Delta_i(k) + \rho_{\max_i \max_k \Delta_i(k)}} \tag{8}$$

$$\Delta_i(k) = |y(k) - x_i(k)| \tag{9}$$

$$\gamma_i = \frac{1}{n}\sum_i^n \xi_i(k) \tag{10}$$

To clarify this issue, the LF-NMR-resolved gel-pore classes were further compared with the nanoindentation-derived C-S-H phases (Fig. 12). A clear positive correspondence was observed between LGP, SGP, and IGP and the fractions of LD, HD, and UHD C-S-H, respectively. This correspondence reflects the intrinsic coupling between gel-pore size and the packing density of the C-S-H network. In ISA-containing pastes, the LF-NMR results showed a progressive redistribution from LGP toward SGP and IGP, indicating refinement of the C-S-H gel structure. This refinement was consistent with the increased fractions of HD and UHD C-S-H identified by nanoindentation, suggesting that the transition from larger to finer gel pores is accompanied by denser C-S-H packing.

Collectively, LF-NMR provides a physically meaningful bridge between pore evolution, C-S-H nanomechanics, and macroscopic strength. The agreement with N_2 adsorption and MIP confirms its reliability for multiscale pore characterization, while the correspondence between gel-pore classes and C-S-H mechanical phases supports the interpretation of LF-NMR gel-pore parameters as strength-relevant descriptors, as shown in Fig. 13. Therefore, porosity, LGP, SGP, and IGP were selected as physically interpretable inputs for the subsequent strength prediction analysis, rather than being used as purely statistical variables.

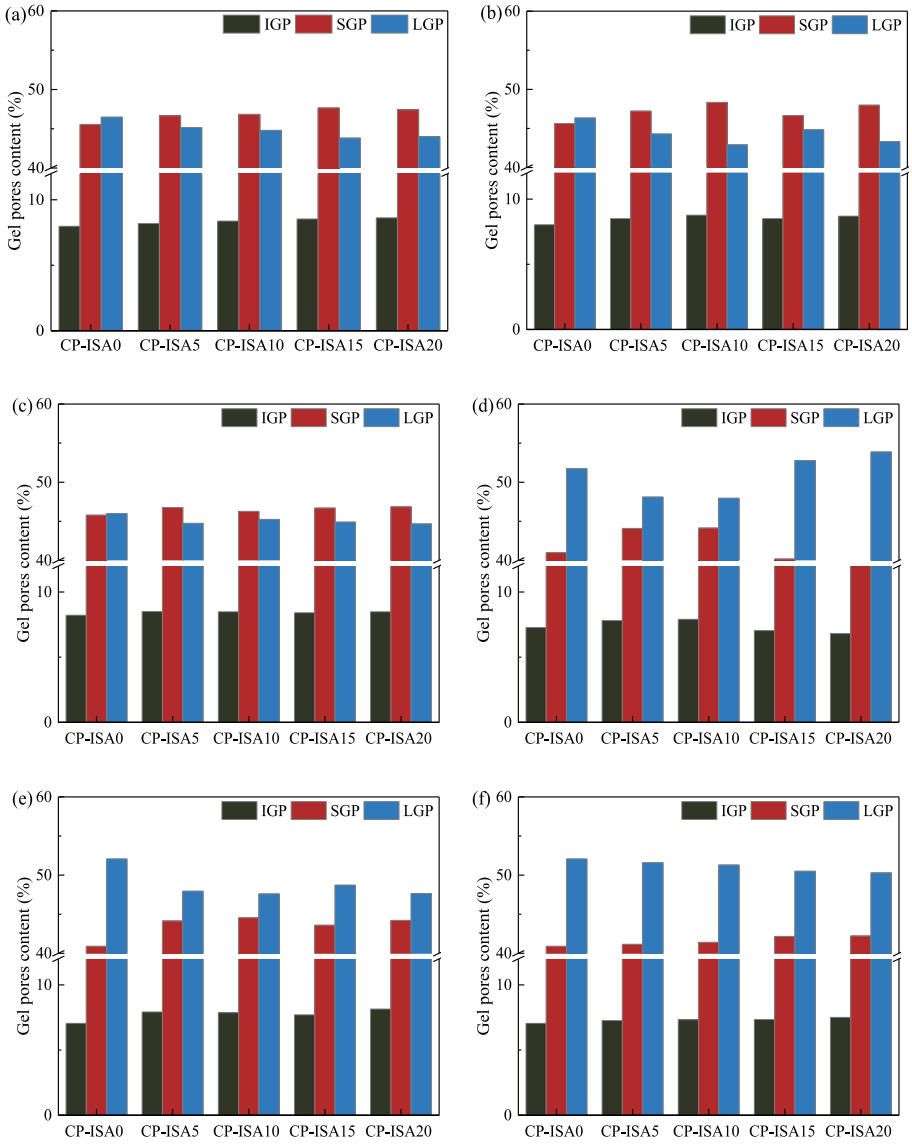

Fig. 11. Gel pore distributions of the cement paste at 1 d (a), 3 d (b), 7 d (c), 28 d (d), 60 d (e), and 90 d (f).

Table 2
Grey relational degrees between pore parameters and compressive strength.

Correlation index	<1 nm	1–3 nm	3–12 nm	12–50 nm	50–100 nm	>100 nm	Porosity
γ_i	0.7209	0.7244	0.7765	0.6851	0.6827	0.6573	0.7363

4.3. Strength prediction based on pore structure

A Bayesian-regularized backpropagation neural network was used for strength prediction under limited-sample conditions. The trainbr algorithm balances fitting accuracy and weight regularization, thereby reducing overfitting and allowing all training samples to be used without an independent validation subset. The number of hidden neurons was determined by five-fold cross-validation within the training set (Qi et al., 2025). To improve prediction stability, seven networks with identical architectures but different initial weights were trained independently, and their averaged output was used as the final prediction. All input variables were normalized before training to reduce scale effects and improve numerical stability (Ma et al., 2024). Based on the analysis in Section 4.2, LF-NMR-derived porosity, LGP, SGP, IGP, and curing age were selected as model inputs. These descriptors are associated with gel-pore refinement and C-S-H packing-density evolution during hydration, and therefore provide physical relevance beyond purely statistical variables. Their inclusion improves the interpretability of the neural network compared with purely data-driven input selection (Qi et al., 2025). The model showed satisfactory predictive performance, with an RMSE below 6 MPa and an (R^2) of 0.94 for the independent test set (Table 3). Although slight overestimation was observed for high-strength samples, the relative errors of all mixtures remained within ±10.60%, which is acceptable given the limited dataset and the sensitivity of gel-pore characteristics to mixture composition and curing age.

4.4. Environmental benefit and cost assessment

The conventional disposal of ISA by landfilling or dumping may

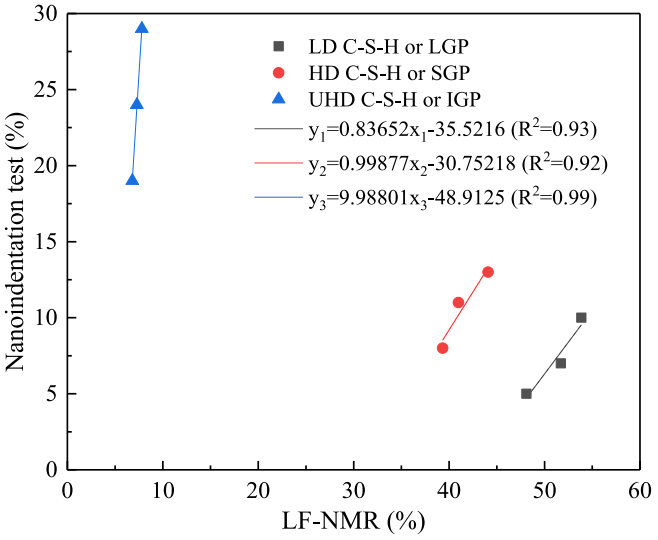

Fig. 12. Relationships between LF-NMR-derived gel-pore classes and nanoindentation-derived C-S-H phases.

cause environmental burdens, including air pollution, water contamination, and ecological degradation. Incorporating ISA into cementitious materials therefore provides a potential route for waste valorization while reducing the economic and environmental impacts of cement-based products. In this section, the economic cost, carbon footprint, and embodied energy of ISA-blended cement pastes were evaluated, as shown in Fig. 14. The unit cost, CO_2 emission factor, and embodied energy of each constituent material were collected from published literature and relevant databases, and the detailed values and corresponding references (Vignesh and Rahim, 2025;Teixeira et al., 2016;Ni et al., 2024;Hu et al., 2023;Gu et al., 2024;Guo et al., 2024) are provided in Table 4.

The impact of ISA incorporation on the economic viability of cement pastes was assessed utilizing both the absolute total cost (C_{cost}) and the strength-normalized cost (C_p):

$$C_{cost} = \sum_{i=1}^{n} N_i \cdot p_i \tag{11}$$

$$C_p = \frac{C_{cost}}{f_c} \tag{12}$$

Where N_i is the unit cost of the i th ingredient as listed in Table 4, p_i is the mass of the i th ingredient as listed in Table 1, and f_c is the 28-day compressive strength of the cement pastes. As shown in Fig. 14(a), the absolute cost decreased linearly from 162.0 USD·m^{-3} for CP-ISA0 to 129.6 USD·m^{-3} for CP-ISA20, owing to the lower unit cost of ISA compared with Portland cement. However, the strength-normalized cost showed a V-shaped trend. The lowest C_p value was obtained for CP-ISA5, reaching 1.32 USD·(MPa·m^3)$^{-1}$, which was 7.04% lower than that of CP-ISA0. Although C_p increased at higher ISA replacement levels because of strength reduction caused by dilution, the value for CP-ISA20 remained lower than that of the control. These results indicate that ISA incorporation can improve the cost-efficiency of cement pastes, with 5% replacement giving the most favorable balance between cost and strength.

To quantify the environmental dividends of ISA utilization, the total CO_2 emissions (C_{weight}) and the strength-normalized carbon footprint (CI) were formulated as follows:

$$C_{weight} = \sum_{i=1}^{n} W_i \cdot p_i \tag{13}$$

$$CI = \frac{C_{weight}}{f_c} \tag{14}$$

Where W_i is the unit carbon emission of the i th ingredient as listed in

Table 3
Comparison between measured and predicted compressive strengths based on pore parameters.

Group	Measured value (MPa)	Predicted value (MPa)	Difference value (MPa)	Error rate (%)
1	81.85	81.59	−0.26	−0.32
2	98.54	108.96	10.42	10.57
3	88.88	93.19	4.31	4.85
4	121.4	123.92	2.52	2.08
5	116.31	114.89	−1.42	−1.22
6	64.58	68.61	4.03	6.24

RMSE: 5.0324 MPa, R^2: 0.94.

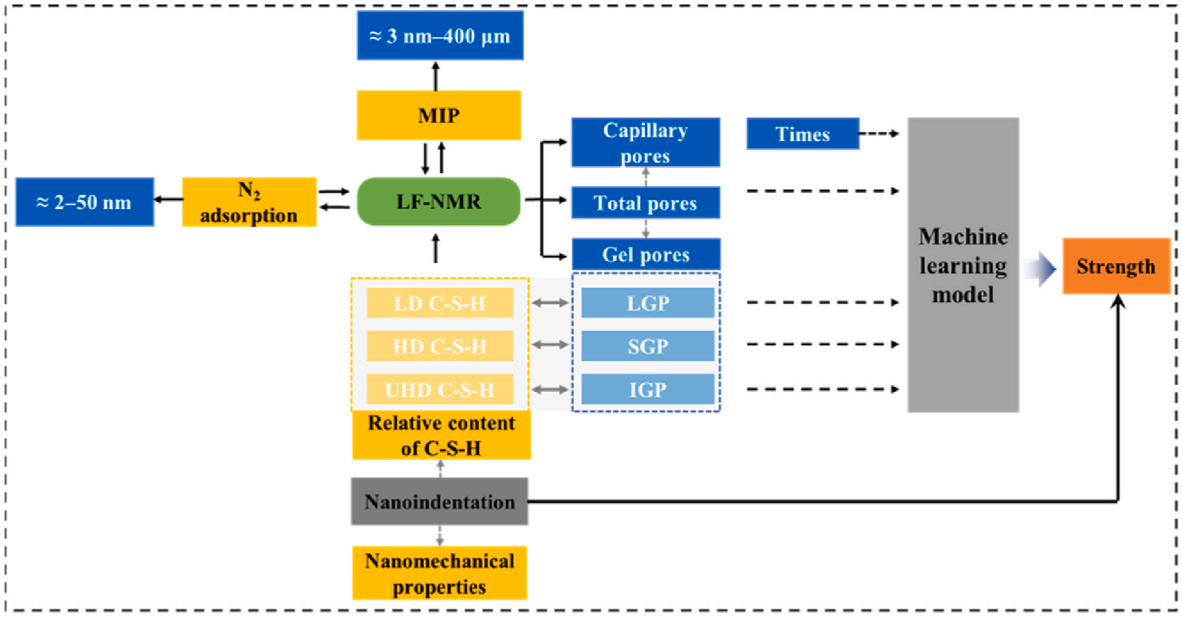

Fig. 13. LF-NMR framework for pore and phase informed strength prediction.

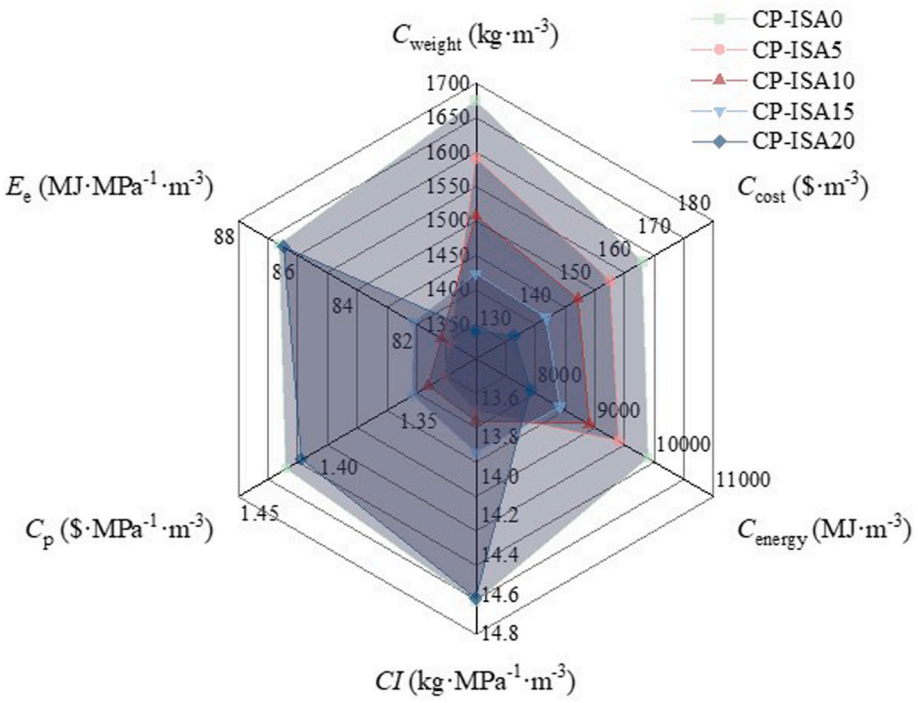

Fig. 14. Economic and environmental indicators of cement pastes containing different ISA contents.

Table 4
The unit cost, CO_2 emission factor, and embodied energy of raw materials.

Material	CO_2 emissions (kg/kg)	Unit cost ($/kg)	Embodied energy (MJ/kg)	Ref.
PC	0.930	0.090	5.50	Vignesh and Rahim (2025); Teixeira et al. (2016)
ISA	2.80×10^{-5}	1.99×10^{-3}	5.94×10^{-3}	
Coral powder (CP)	0.011	-	-	Ni et al. (2024)
White dolomite powder (WDP)	0.029	0.005	-	Hu et al. (2023)
Steel slag powder (SSP)	0.019	0.023	-	Gu et al. (2024)
Ground granulated blastfurnace slag (GGBS)	0.020	0.100	-	Guo et al. (2024)

Table 4. As shown in Fig. 14(b), the total carbon footprint decreased from 1674 kg m^{-3} for CP-ISA0 to 1339.2 kg m^{-3} for CP-ISA20, corresponding to a 20% reduction. This decrease resulted directly from the partial replacement of cement by ISA. However, the *CI* values showed that carbon reduction should be evaluated together with mechanical performance. The CI decreased from 14.64 kg·(MPa·m^3)$^{-1}$ for CP-ISA0 to the minimum value of 13.67 kg·(MPa·m^3)$^{-1}$ for CP-ISA5, representing a 6.63% reduction. At higher replacement levels, the *CI* values increased slightly to 13.72–14.62 kg·(MPa·m^3)$^{-1}$, mainly due to the loss in compressive strength. Therefore, although higher ISA contents continuously reduced absolute CO_2 emissions, 5% ISA provided the best carbon efficiency.

The energy-saving potential of ISA was further investigated by evaluating the non-renewable energy consumption (NREC, functionally equivalent to total embodied energy) and the strength-normalized embodied energy (E_e):

$$C_{energy} = \sum_{i=1}^{n} E_i \cdot p_i \tag{15}$$

$$E_e = \frac{C_{energy}}{f_c} \tag{16}$$

Where E_i is the unit embodied energy of the i th ingredient as listed in Table 4. As shown in Fig. 14(c), the absolute NREC decreased linearly from 9900 MJ m^{-3} for CP-ISA0 to 7922.14 MJ m^{-3} for CP-ISA20, reflecting the reduced cement content. Similar to the cost and carbon results, E_e identified CP-ISA5 as the optimal mixture. The E_e value decreased from 86.61 MJ·(MPa·m^3)$^{-1}$ for CP-ISA0 to 80.87 MJ·(MPa·m^3)$^{-1}$ for CP-ISA5. Even at 20% ISA replacement, E_e remained 0.17% lower than that of the control. Overall, ISA incorporation effectively reduced the cost, carbon footprint, and embodied energy of cement pastes. Nevertheless, considering both sustainability indicators and mechanical performance, 5% ISA replacement was the most eco-efficient content.

To benchmark the sustainability of ISA against other mineral admixtures, the same methodology was used to calculate CO_2 emissions, material costs, and the corresponding *CI* and C_p indices for mixtures containing alternative SCMs reported in references (Vignesh and Rahim, 2025; Teixeira et al., 2016; Ni et al., 2024; Hu et al., 2023; Gu et al., 2024; Guo et al., 2024) (Fig. 15). At comparable replacement levels, ISA-blended mixtures generally showed lower absolute CO_2 emissions, material costs, *CI*, and C_p than mixtures incorporating other mineral admixtures. Compared with CP10 and WDP10, CP-ISA10 reduced CO_2 emissions by 0.13% and 0.35%, respectively, while decreasing *CI* by 47.54% and 73.41%. Similarly, compared with CP15, SSP15, and GGBS15, CP-ISA15 reduced CO_2 emissions by 0.21%–0.65% and *CI* by 48.50%–57.00%. In terms of economic performance, CP-ISA10 reduced the absolute cost and C_p by 5.81% and 74.83%, respectively, relative to WDP10. CP-ISA15 also showed 4.11%–4.35% lower costs and 54.65%–58.60% lower C_p than SSP15 and GGBS15, while CP-ISA20 outperformed WDP20 with reductions of 12.20% in cost and 71.72% in C_p. These results further support the potential of ISA as a low-cost and low-carbon SCM for sustainable cementitious materials. Nevertheless, future studies should use unified functional units, consistent mixture

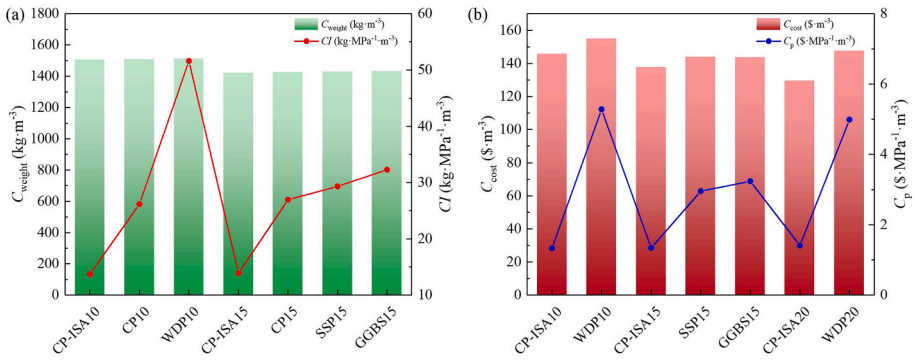

Fig. 15. Comparison of environmental (a) and economic benefits (b) of this study with references (Vignesh and Rahim, 2025; Teixeira et al., 2016; Ni et al., 2024; Hu et al., 2023; Gu et al., 2024; Guo et al., 2024).

designs, and more comprehensive life-cycle inventory data to enable a more rigorous comparison among different SCMs.

5. Conclusion

This study validated LF-NMR for multiscale pore characterization through comparison with MIP and N_2 adsorption. Linking LF-NMR-resolved gel-pore classes with nanoindentation-derived C-S-H phases established a cross-scale relationship among pore refinement, nanomechanical evolution, and strength development, supporting the mechanistic evaluation of ISA as a potential supplementary cementitious material. The main conclusions are as follows:

(1) LF-NMR effectively captured the hydration evolution and pore refinement of cement pastes at different curing ages. The decline in $\overline{T_2}$ values reflected continuous densification of the pore system, and the hydration trends measured by LF-NMR were consistent with those obtained from BSE-based hydration degree. LF-NMR provides stable, non-destructive, and age-continuous measurements that complement traditional methods.
(2) A multi-technique comparison confirmed the reliability of LF-NMR for the multiscale pore characterization. LF-NMR showed good agreement with N_2 adsorption in the gel-pore range and with MIP for the capillary pores. Owing to its wider detection range, LF-NMR provides a more comprehensive description of pore structure evolution than individual conventional methods.
(3) LF-NMR enabled quantitative tracking of IGP, SGP, and LGP evolution, thereby revealing the refinement of the C-S-H gel-pore structure. The redistribution from LGP toward SGP and IGP was closely associated with the development of denser C-S-H mechanical phases identified by nanoindentation. This correspondence establishes a mechanistic link between gel-pore refinement and C-S-H nanomechanical phase evolution.
(4) A Bayesian-regularized BP neural network using LF-NMR-derived porosity, LGP, SGP, IGP, and curing age as inputs achieved an R^2 of 0.94 and prediction errors within ±10.60%. Because these pore descriptors are linked to C-S-H gel-pore refinement and nanomechanical phase evolution, they provide physically meaningful inputs for strength prediction under limited-sample conditions.
(5) ISA incorporation significantly reduced the cost, carbon footprint, and embodied energy of cement pastes. Although the absolute sustainability indicators decreased continuously with increasing ISA content, the strength-normalized assessment identified 5% ISA as the optimal replacement level, achieving the best balance between mechanical performance and sustainability.

Collectively, LF-NMR provides a reliable method for characterizing multiscale pore evolution and relating gel-pore changes to the C-S-H mechanical phases and compressive strength. Combined with nanoindentation and machine learning, this method enables microstructural evaluation and strength prediction using physically meaningful pore parameters. For ISA-blended cement pastes, the results show that moderate ISA addition refines the gel-pore structure and promotes the formation of denser C-S-H phases, thereby improving the later-age strength and eco-efficiency. However, the conclusions are limited to the ISA source, mixture design, and paste system examined in this study. Future studies should consider ISA from different sources, improve its reactivity and effective replacement level, and verify the observed pore-phase strength relationships in mortar and concrete. The effects of ISA on shrinkage, creep, and durability also require further investigation.

CRediT authorship contribution statement

Zi-jun Li: Data curation, Methodology, Writing – original draft. **Zhi-hai He:** Conceptualization, Funding acquisition, Project administration, Writing – review & editing. **Fu-qiang He:** Writing – review & editing. **Hanbing Zhao:** Writing – review & editing. **Juan Wang:** Supervision, Visualization, Writing – review & editing. **Arezou Babaahmadi:** Writing – review & editing.

Declaration of competing interest

The authors declare that they have no known competing financial interests or personal relationships that could have appeared to influence the work reported in this paper.

Acknowledgement

The authors would like to acknowledge the Central Government Funding Program for Guiding Local Science and Technology Development (2025ZY01028) for their financial support for the work presented in this paper.

Data availability

Data will be made available on request.

References

Cano-Barrita, P.D.J., Marble, A.E., Balcom, B.J., et al., 2009. Embedded NMR sensors to monitor evaporable water loss caused by hydration and drying in Portland cement mortar. Cement Concr. Res. 39 (4), 324–328.
Chen, B., Ye, G., 2024. The role of water-treated municipal solid waste incineration (MSWI) bottom ash in microstructure formation and strength development of blended cement pastes. Cement Concr. Res. 178, 107440.
Chen, W., Li, Y., Zhou, Y., et al., 2024. Impact of basic oxygen furnace slag on the hydration microstructure, mechanical properties, and carbon emissions of supersulfated cement. Constr. Build. Mater. 432, 136673.

Ectors, D., Goetz-Neunhoeffer, F., Hergeth, W., et al., 2016. In situ 1H-TD-NMR: quantification and microstructure development during the early hydration of alite and OPC. Cement Concr. Res. 79, 366–372.
Georget, F., Sui, S., Wilson, W., et al., 2024. Reconciliation of pore structure characterization methods: the simple case of PC-limestone cement pastes. Cement Concr. Res. 184, 107624.
Gu, X., Wang, H., Liu, J., et al., 2024. Synergistic effects of steel slag and metakaolin in cementitious systems: packing properties, strength, and microstructure. Constr. Build. Mater. 411, 134395.
Guo, W., Yao, W., Liang, G., et al., 2024. Mechanical properties, microstructure and life-cycle assessment of eco-friendly cementitious materials containing circulating fluidized bed fly ash and ground granulated blast furnace slag. J. Build. Eng. 95, 110293.
Hay, R., Li, J., Celik, K., 2020. Influencing factors on micromechanical properties of calcium (alumino) silicate hydrate C-(A-) SH under nanoindentation experiment. Cement Concr. Res. 134, 106088.
He, Z., Li, L., Du, S., 2017. Creep analysis of concrete containing rice husk ash. Cement Concr. Compos. 80, 190–199.
He, Z., Li, Z., He, F., et al., 2024. Utilization of incense stick ash as a supplementary cementitious material: effects on strength, cement chemistry, and sustainability. Constr. Build. Mater. 451, 138695.
He, Z., Shen, M., Shi, J., et al., 2022. Recycling coral waste into eco-friendly UHPC: mechanical strength, microstructure, and environmental benefits. Sci. Total Environ. 836, 155424.
Hu, H., Yao, W., Wei, Y., 2023. Recycling waste dolomite powder in cement paste: early hydration process, microscale characteristics, and life-cycle assessment. Sci. Total Environ. 902, 166008.
Jennings, H.M., 2008. Refinements to colloid model of CSH in cement: cm-II. Cement Concr. Res. 38 (3), 275–289.
Ji, Y., Sun, Z., Yang, X., et al., 2015. Assessment and mechanism study of bleeding process in cement paste by 1H low-field NMR. Constr. Build. Mater. 100, 255–261.
Jiang, Z., Pan, Y., Fu, C., et al., 2023. Three-dimensional pore structure characterization of cement paste by X-ray computed tomography (XCT) and focused ion beam/scanning electron microscopy (FIB/SEM). Constr. Build. Mater. 383, 131379.
Kunhi, Mohamed A., Moutzouri, P., Berruyer, P., et al., 2020. The atomic-level structure of cementitious calcium aluminate silicate hydrate. J. Am. Chem. Soc. 142 (25), 11060–11071.
Lam, W.L., Cai, Y., Sun, K., et al., 2024. Roles of ultra-fine waste glass powder in early hydration of Portland cement: hydration kinetics, mechanical performance, and microstructure. Constr. Build. Mater. 415, 135042.
Li, L., Liu, Z., Liu, W., et al., 2025. Microstructure and transport properties of cement mortar made with recycled fine ceramic aggregates. Dev. Built Environ. 22, 100643.
Liu, H., Sun, Z., Yang, J., et al., 2021. A novel method for semi-quantitative analysis of hydration degree of cement by 1H low-field NMR. Cement Concr. Res. 141, 106329.
Liu, J., Xu, S., Zeng, Q., 2026. Multi-scale characterization of fracture properties of cement-based materials via scratch test. Constr. Build. Mater. 512, 145350.
Liu, K., Yu, J., Chen, Y., et al., 2024. Preparation of cellulose fibre-sheets and its impact on pore connectivity of cement paste during early hydration. Constr. Build. Mater. 411, 134535.
Lothenbach, B., Scrivener, K., Hooton, R.D., 2011. Supplementary cementitious materials. Cement Concr. Res. 41 (12), 1244–1256.
Lu, J., Shen, P., Zheng, H., et al., 2021. Development and characteristics of ultra high-performance lightweight cementitious composites (UHP-LCCs). Cement Concr. Res. 145, 106462.
Lyu, K., She, W., Miao, C., et al., 2019. Quantitative characterization of pore morphology in hardened cement paste via SEM-BSE image analysis. Constr. Build. Mater. 202, 589–602.
Ma, S., Zhang, Z., Liu, X., et al., 2023. Quantitative characterization of the early hydration of magnesium potassium phosphate cement: In-situ experiment with low field NMR. Constr. Build. Mater. 377, 131066.
Ma, Y., Liu, M., Yang, L., et al., 2024. A BP neural network prediction model of compressive strength of green bricks in the Ming dynasty based on CT scanning technique. Constr. Build. Mater. 435, 136873.
Marinković, S., Carević, V., Dragaš, J., 2021. The role of service life in life cycle assessment of concrete structures. J. Clean. Prod. 290, 125610.
Nestle, N., Galvosas, P., Kärger, J., 2007. Liquid-phase self-diffusion in hydrating cement pastes—results from NMR studies and perspectives for further research. Cement Concr. Res. 37 (3), 398–413.
Ni, Y., Shi, J., He, Z., et al., 2024. Synergistic effect of coral sand and coral powder on the performance of eco-friendly mortar. Constr. Build. Mater. 411, 134468.
Patel, S., Orlov, A., Ariyachandra, E., et al., 2021. Effect of flue gas temperature on NO2 adsorption by aged recycled concrete waste: DRIFTS, TGA and BET study. Chem. Eng. J. 420, 130413.
Peng, Y., Unluer, C., 2023. Modeling the mechanical properties of recycled aggregate concrete using hybrid machine learning algorithms. Resour. Conserv. Recycl. 190, 106812.
Powers, T.C., Copeland, L.E., Mann, H.M., 1959. Capillary Continuity or Discontinuity in Cement Pastes[J]. pca bullentin.
Qi, H., Guan, X., Chen, Q., et al., 2025. Physics descriptors enhanced Bayesian learning method for permeability of random media under sparse data. Eng. Appl. Artif. Intell. 143, 109929.
She, A., Yao, W., 2010. Research on hydration of cement at early age by proton NMR. J. Build. Mater. 13 (3), 376–379.
Sorelli, L., Constantinides, G., Ulm, F., et al., 2008. The nano-mechanical signature of ultra high performance concrete by statistical nanoindentation techniques. Cement Concr. Res. 38 (12), 1447–1456.
Sun, Y., Lu, J., Poon, C.S., 2022. Strength degradation of seawater-mixed alite pastes: an explanation from statistical nanoindentation perspective. Cement Concr. Res. 152, 106669.
Teixeira, E.R., Mateus, R., Camoes, A.F., et al., 2016. Comparative environmental life-cycle analysis of concretes using biomass and coal fly ashes as partial cement replacement material. J. Clean. Prod. 112, 2221–2230.
Vignesh, R., Rahim, A.A., et al., 2025. Optimization and potential utilization of agro-industrial by-products as binders in quaternary blended pastes—A sustainable approach. Case Stud. Constr. Mater. 22, e04588.
Xiao, J., Zou, S., Poon, C.S., et al., 2025. We use 30 billion tonnes of concrete each year—here's how to make it sustainable. Nature 638 (8052), 888–890.
Xue, S., Meng, F., Zhang, P., et al., 2020. Influence of water re-curing on microstructure of heat-damaged cement mortar characterized by low-field NMR and MIP. Constr. Build. Mater. 262, 120532.
Yin, T., Jin, L., Liu, K., et al., 2024. Fractal evolution model of proton spatial distribution in low water/binder cement-based composites (LW/B-CC) during early-age hydration process. Constr. Build. Mater. 427, 136287.
You, X., Wen, R., Qiu, Y., et al., 2026. Utilizing desert sand and industrial by-products for developing cement-free highly thermal conductive, low-cost materials for data center buildings. Constr. Build. Mater. 534, 146849.
Zeng, Q., Xu, C., Qiu, Y., et al., 2026. Mechanistic understanding of hydration process and microstructure of Portland cement altered by in-situ polymerization. Cement Concr. Res. 206, 108266.
Zhan, P., Wang, J., Zhao, H., et al., 2024. Impact of synthetic CSH seeds on early hydration and pore structure evolution of cement pastes: a study by 1H low-field NMR and path analysis. Cement Concr. Res. 175, 107376.
Zhang, A., Ge, Y., Yang, W., et al., 2023a. New insight of solvent-replacement-induced damage to pores of cement stone by comparison with 1H NMR relaxometry, mercury intrusion porosimetry, and nitrogen adsorption. Constr. Build. Mater. 409, 133981.
Zhang, Z., Qin, J., Ma, Z., et al., 2023b. Comparison of three different deconvolution methods for analyzing nanoindentation test data of hydrated cement paste. Cement Concr. Compos. 138, 104990.
Zhou, C., Ren, F., Wang, Z., et al., 2017. Why permeability to water is anomalously lower than that to many other fluids for cement-based material? Cement Concr. Res. 100, 373–384.